of photochemical and environmental stresses. X-ray diffraction (XRD) (Fig. 4B) analysis showed that performance degradation corresponded to the decomposition of the crystalline perovskite material into PbI_2, which was not observed for the fully coated devices (see section 6 in the supplementary materials).

Given the stabilizing effect of the fluoropolymeric coating applied on both sides of the cells, a second aging test was designed to verify the stability of the front/back-coated PSCs under real outdoor atmospheric conditions, where temperature variations, precipitation phenomena, and pollution are typically encountered. A batch of five cells was exposed on the terrace of the Politecnico di Torino building in Turin (45°06′N, 7°66′E), located in northwest Italy, in a humid subtropical climate zone from October to December 2015. The PSCs were subjected to highly variable climatic conditions, as outdoor temperatures ranged from −3° to +27°C, and 27 out of 92 days were characterized by heavy rain and storms (*33*), as shown in Fig. 4C. The front/back-coated PSCs exhibited long-term stability retaining 95% of their initial efficiency after this test by (i) protecting the perovskite from UV radiation, converting it into exploitable visible photons; (ii) acting as a moisture barrier, thus preventing hydrolytic phenomena of the perovskite material; and (iii) keeping the front electrode clean by means of the easy-cleaning characteristics of this fluorinated polymer. Similar results were found for outdoor tests performed during Summer 2016, and the data collected are available in section 7 in the supplementary materials.

To demonstrate the water resistance of the photopolymerized fluorinated coatings, we kept five solar cells for 1 month in a closed chamber in the presence of a beaker containing boiling water (95% RH, fig. S1C), and the photovoltaic response was evaluated once a week. After 1 month, four of the five cells withstood the strong aging conditions and remarkably retained 96 ± 2% of their initial PCE. Only one device lost 95% of its initial efficiency after the first week. After inspection, we found a small area on the back side of the solar cell not thoroughly coated by the fluoropolymeric layer. The nonhomogeneous deposition of the coating caused a gradual hydrolysis of the underlying perovskite layer. We also dipped the front/back-coated devices into water. After 1 day of immersion, no changes in their photovoltaic performance were observed.

REFERENCES AND NOTES

1. H. S. Kim *et al.*, *Sci. Rep.* **2**, 591 (2012).
2. M. M. Lee, J. Teuscher, T. Miyasaka, T. N. Murakami, H. J. Snaith, *Science* **338**, 643–647 (2012).
3. H. Zhou *et al.*, *Science* **345**, 542–546 (2014).
4. M. Liu, M. B. Johnston, H. J. Snaith, *Nature* **501**, 395–398 (2013).
5. J. Burschka *et al.*, *Nature* **499**, 316–319 (2013).
6. National Center for Photovoltaics (NCPV) at the National Renewable Energy Laboratory (NREL); http://www.nrel.gov/ncpv (accessed July 2016).
7. N. G. Park, *Mater. Today* **18**, 65–72 (2015).
8. J. Seo, J. H. Noh, S. I. Seok, *Acc. Chem. Res.* **49**, 562–572 (2016).
9. H. S. Jung, N. G. Park, *Small* **11**, 10–25 (2015).
10. T. A. Berhe *et al.*, *Energy Environ. Sci.* **9**, 323–356 (2016).
11. Y. Rong, L. Liu, A. Mei, X. Li, H. Han, *Adv. Energy Mater.* **5**, 1501066 (2015).
12. T. Leijtens *et al.*, *Adv. Energy Mater.* **5**, 1500963 (2015).
13. J. P. Correa Baena *et al.*, *Energy Environ. Sci.* **8**, 2928–2934 (2015).
14. J. P. Correa-Baena *et al.*, *Adv. Mater.* **28**, 5031–5037 (2016).
15. H. C. Weerasinghe, Y. Dkhissi, A. D. Scully, R. A. Caruso, Y. B. Cheng, *Nano Energy* **18**, 118–125 (2015).
16. I. Hwang, I. Jeong, J. Lee, M. J. Ko, K. Yong, *ACS Appl. Mater. Interfaces* **7**, 17330–17336 (2015).
17. M. Kaltenbrunner *et al.*, *Nat. Mater.* **14**, 1032–1039 (2015).
18. J. You *et al.*, *Nat. Nanotechnol.* **11**, 75–81 (2016).
19. K. Domanski *et al.*, *ACS Nano* **10**, 6306–6314 (2016).
20. X. Li *et al.*, *Nat. Chem.* **7**, 703–711 (2015).
21. A. Mei *et al.*, *Science* **345**, 295–298 (2014).
22. L. Zhang *et al.*, *J. Mater. Chem. A* **3**, 9165–9170 (2015).
23. W. Li *et al.*, *Energy Environ. Sci.* **9**, 490–498 (2016).
24. Materials and methods are available as supplementary materials on *Science* Online.
25. F. Bella *et al.*, *Adv. Funct. Mater.* **26**, 1127–1137 (2016).
26. L. R. Wilson, B. S. Richards, *Appl. Opt.* **48**, 212–220 (2009).
27. D. Bi *et al.*, *Sci. Adv.* **2**, e1501170 (2016).
28. F. Giordano *et al.*, *Nat. Commun.* **7**, 10379 (2016).
29. D. Liu, T. L. Kelly, *Nat. Photonics* **8**, 133–138 (2014).
30. J.-H. Im, I.-H. Jang, N. Pellet, M. Grätzel, N.-G. Park, *Nat. Nanotechnol.* **9**, 927–932 (2014).
31. G. Griffini, M. Levi, S. Turri, *Sol. Energy Mater. Sol. Cells* **118**, 36–42 (2013).
32. G. Griffini, M. Levi, S. Turri, *Prog. Org. Coat.* **77**, 528–536 (2014).
33. Il Meteo; http://www.ilmeteo.it/meteo/Torino (accessed September 2016).

ACKNOWLEDGMENTS

Authors from EPFL thank the Swiss National Science Foundation, the NRP 70 "Energy Turnaround," the 9th call proposal 906 (CONNECT PV), SNF-NanoTera, and the Swiss Federal Office of Energy (SYNERGY) for financial support. All data used in this study are included in the main text and in the supplementary materials.

SUPPLEMENTARY MATERIALS

www.sciencemag.org/content/354/6309/203/suppl/DC1
Materials and Methods
Supplementary Text Sections 1 to 7
Figs. S1 to S8
References (*34*–*40*)

21 June 2016; accepted 20 September 2016
Published online 29 September 2016
10.1126/science.aah4046

SOLAR CELLS

Incorporation of rubidium cations into perovskite solar cells improves photovoltaic performance

Michael Saliba,[1]*† Taisuke Matsui,[1,2]† Konrad Domanski,[1]† Ji-Youn Seo,[1] Amita Ummadisingu,[1] Shaik M. Zakeeruddin,[1] Juan-Pablo Correa-Baena,[3] Wolfgang R. Tress,[1] Antonio Abate,[1] Anders Hagfeldt,[3] Michael Grätzel[1]*

All of the cations currently used in perovskite solar cells abide by the tolerance factor for incorporation into the lattice. We show that the small and oxidation-stable rubidium cation (Rb^+) can be embedded into a "cation cascade" to create perovskite materials with excellent material properties. We achieved stabilized efficiencies of up to 21.6% (average value, 20.2%) on small areas (and a stabilized 19.0% on a cell 0.5 square centimeters in area) as well as an electroluminescence of 3.8%. The open-circuit voltage of 1.24 volts at a band gap of 1.63 electron volts leads to a loss in potential of 0.39 volts, versus 0.4 volts for commercial silicon cells. Polymer-coated cells maintained 95% of their initial performance at 85°C for 500 hours under full illumination and maximum power point tracking.

Low-cost perovskite solar cells (PSCs) have achieved certified power conversion efficiencies (PCEs) of 22.1% (*1*). The organic-inorganic perovskites used for photovoltaics (PV) have an AMX_3 formula that comprises a monovalent cation, A [cesium Cs^+, methylammonium (MA) $CH_3NH_3^+$, or formamidinium (FA) $CH_3(NH_2)_2^+$]; a divalent metal, M (Pb^{2+} or Sn^{2+}); and an anion, X (Cl^-, Br^-, or I^-). The highest-efficiency perovskites are Pb-based with mixed MA/FA cations and Br/I halides (*2*–*4*). Recently, Cs was used to explore more complex cation combinations: Cs/MA, Cs/FA, and Cs/MA/FA (*5*–*9*). These perovskite formulations exhibit unexpected properties. For example, Cs/FA mixtures suppress halide segregation, enabling band gaps for perovskite/silicon tandems (*10*). The Cs/MA/FA-based solar cells are more reproducible and thermally stable than MA/FA mixtures (*9*).

In general, increasing the perovskite complexity is motivated by the need to improve stability by adding more inorganic elements and increasing the entropy of mixing, which can stabilize ordinarily unstable materials (such as the "yellow," non-photoactive phase of $FAPbI_3$ that can be avoided by using small amounts of the otherwise unstable

[1]Laboratory of Photonics and Interfaces, École Polytechnique Fédérale de Lausanne, Station 6, CH-1015 Lausanne, Switzerland. [2]Advanced Research Division, Materials Research Laboratory, Panasonic Corporation, 1006 Kadoma, Kadoma City, Osaka 571-8501, Japan. [3]Laboratory of Photomolecular Science, École Polytechnique Fédérale de Lausanne, Station 6, CH-1015 Lausanne, Switzerland.
***Corresponding author. Email: michael.saliba@epfl.ch (M.S.); michael.graetzel@epfl.ch (M.G.)** †These authors contributed equally to this work.

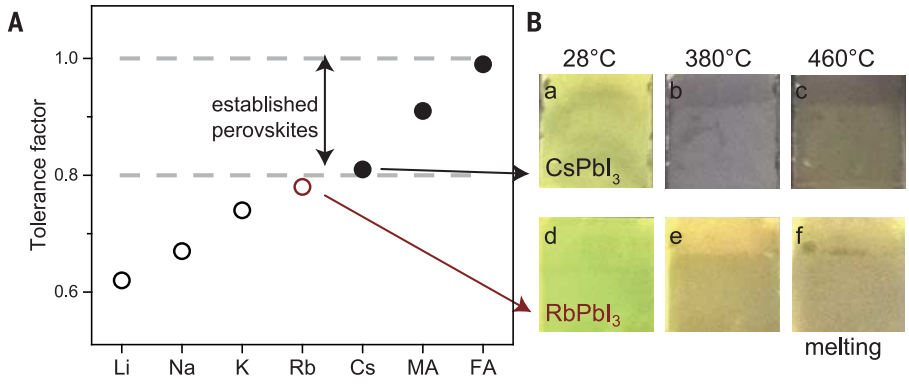

Fig. 1. Tolerance factor and perovskites at different temperatures. (**A**) Tolerance factor of $APbI_3$ perovskite with the oxidation-stable A (Li, Na, K, Rb, or Cs) and MA or FA (see table S1 for detailed calculations and ionic radii). Empirically, perovskites with a tolerance factor between 0.8 and 1.0 (dashed lines) show a photoactive black phase (solid circles) as opposed to nonphotoactive phases (open circles). Rb (red open circle) is very close to this limit, making it a candidate for integration into the perovskite lattice. (**B**) $CsPbI_3$ [(a) to (c)] and $RbPbI_3$ [(d) to (f)] at 28°, 380°, or 460°C. Irreversible melting for both compounds occurs at 460°C. $RbPbI_3$ never shows a black phase.

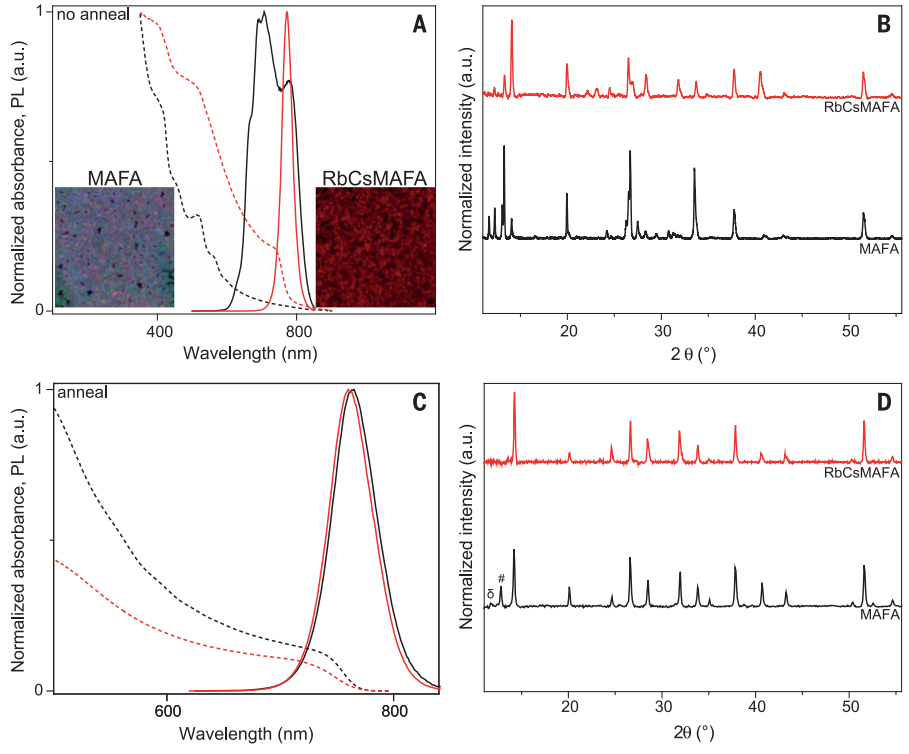

Fig. 2. Characterization of unannealed and annealed films. (**A**) UV-vis (dashed lines) and PL (solid lines) of unannealed MAFA (black) and RbCsMAFA (red) films. The inset images show fluorescence microscopy measurements (image size ~26 μm × 26 μm) of MAFA and RbCsMAFA films. Each image is an overlay of three emission ranges sampled from 640 to 650 nm (assigned as green), 680 to 690 nm (blue), and 725 to 735 nm (red). The colors were chosen to ensure easily discernible features. (**B**) XRD data of the unannealed MAFA and RbCsMAFA films. (**C**) UV-vis (dashed lines) and PL (solid lines) of MAFA (black) and RbCsMAFA (red) films annealed at 100°C for 1 hour. (**D**) XRD data of the annealed MAFA and RbCsMAFA films. The PbI_2 and yellow-phase peaks are denoted as # and δ, respectively.

$CsPbI_3$) (*6*, *7*). However, all combinations of Cs, MA, and FA cations were selected because each individually forms a photoactive perovskite "black" phase (*11*–*13*).

Further progress requires exploration of a wider circle of cations. Unfortunately, most monovalent cations are mismatched to sustain a photoactive $APbI_3$ perovskite with an appropriate Goldschmidt tolerance factor [$t = (r_A + r_I)/\sqrt{2}\ (r_{Pb} + r_I)$, where r is ionic radius] between 0.8 and 1.0 (*14*, *15*), rendering almost all elemental cations too small for consideration. We illustrate this point in Fig. 1A, which shows tolerance factor calculations for the alkali metals (Li, Na, K, Rb, Cs) as well as MA and FA (see table S1 for numeric values and ionic radii). We selected specifically the alkali metals that are oxidation-stable monovalent cations, as these would have a stability advantage over oxidation-prone Pb/Sn mixtures that have distorted material electronic properties (*16*).

The tolerance factor shows that only $CsPbI_3$, $MAPbI_3$, and $FAPbI_3$ fall into the range of "established perovskites" with a black phase. Li, Na, and K are clearly outside of the range, whereas $RbPbI_3$ only misses by a small margin. The ionic radii of Cs and Rb are 167 pm and 152 pm, respectively. This small difference still has a large impact, with $RbPbI_3$ and $CsPbI_3$ drawing the demarcation line between photoactive black perovskite and photoinactive yellow nonperovskite phases. As shown by heating $CsPbI_3$ and $RbPbI_3$ films at different temperatures (Fig. 1B), both films are yellow at 28°C; upon heating to 380°C, only $CsPbI_3$ turns black, whereas $RbPbI_3$ remains yellow. At 460°C, both films start melting irreversibly, without $RbPbI_3$ ever showing a black phase; this is consistent with the observations of Trots and Myagkota (*17*). Thus, only $CsPbI_3$ has a black phase, which explains why Rb has so far not been used for PSCs despite its desirable oxidation stability.

In this work, we propose embedding Rb^+, only slightly smaller than Cs^+, into a photoactive perovskite phase using multiple A-cation formulations. We retain FA as the majority cation because of the beneficial, red-shifted band gap. We identify four previously unexplored combinations: RbFA, RbCsFA, RbMAFA, and RbCsMAFA. In (*18*) and figs. S1 to S3, following the antisolvent approach pioneered by Jeon *et al.* (*2*), we present device data on a glass/fluorine-doped tin oxide/compact TiO_2/mesoporous TiO_2/perovskite/spiro-OMeTAD [2,2′,7,7′-tetrakis(*N*,*N*-di-*p*-methoxyphenylamine)-9,9′-spirobifluorene]/Au architecture. [See fig. S4A for a cross-sectional scanning electron microscopy (SEM) image and fig. S4C for an image of typical devices.] All preparation details are given in (*18*). We use the nomenclature of RbFA, RbCsFA, RbMAFA, and RbCsMAFA to denote the entire perovskite compounds at the optimized values found in (*18*) (usually achieved with an addition of 5 to 10% Rb).

Reasonable device performances were reached with RbFA (14%), RbCsFA (19.3%), RbMAFA (19.2%) [comparable to CsFA (20%)], and CsMAFA (19.2%), as shown in figs. S1 to S3 (measured on a device area of 0.16 cm^2). Thus, Rb can stabilize the black phase of FA perovskite and be integrated into PSCs, despite not being suitable as a pure $RbPbI_3$ compound. Surprisingly, RbCsMAFA (with 5% Rb; fig. S3) resulted in PCEs of 20.6%, with an open-circuit voltage V_{oc} of 1186 mV (*18*). Hence, we focus below on RbCsMAFA to substantiate the impact of the Rb^+ integration approach for PSCs.

We investigated the starting condition of the crystallization process for the RbCsMAFA compound

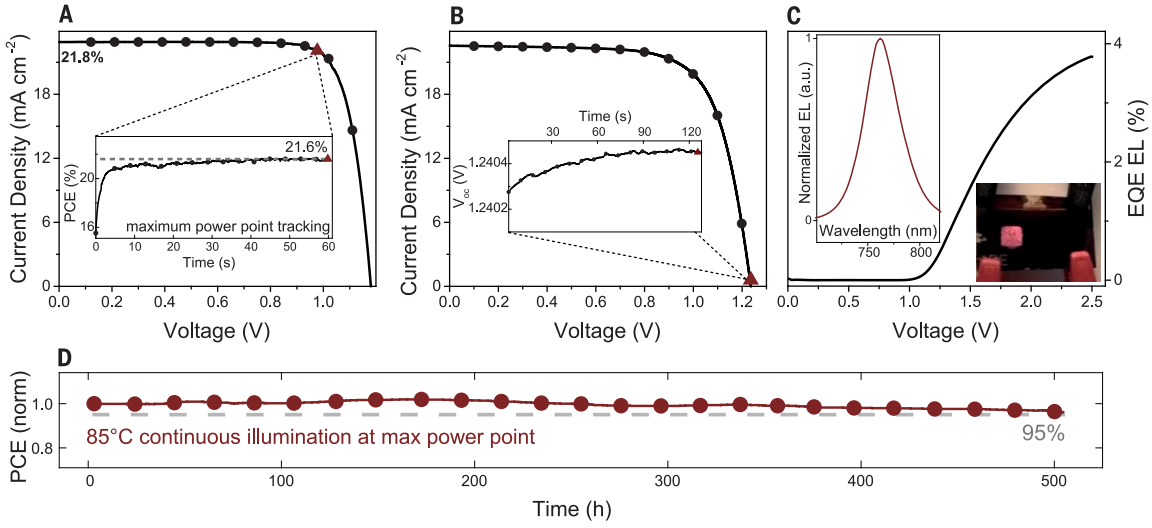

Fig. 3. Efficiency, open-circuit voltage, electroluminescence, and high-temperature stability of the best-performing RbCsMAFA solar cell. (**A**) Current density–voltage (*J-V*) curve, taken at 10 mV s^{-1} scan rate, of the solar cell with 21.8% efficiency (V_{oc} = 1180 mV, J_{sc} = 22.8 mA cm^{-2}, and FF = 81%). The forward and reverse scan is shown in table S2. The inset shows the scan rate–independent MPP tracking for 60 s, resulting in a stabilized efficiency of 21.6% at 977 mV and 22.1 mA cm^{-2} (displayed as triangles in the *J-V* and MPP scans). (**B**) *J-V* curve of the highest-V_{oc} device. The inset shows the V_{oc} over 120 s, resulting in 1240 mV (displayed as the red triangles in the *J-V* and V_{oc} scans). (**C**) EQE electroluminescence (EL) as a function of voltage. The left inset shows the corresponding EL spectrum over wavelength. The right inset shows a solar cell (device size ~1.4 cm × 2.8 cm) with two active areas. The left area is operated as an LED displaying a clearly visible red emission even under ambient light. At the same time, the right area can be operated as a solar cell or a photodetector. (**D**) Thermal stability test of a perovskite solar cell. The device was aged for 500 hours at 85°C under continuous full illumination and MPP tracking in a nitrogen atmosphere (red curve, circles). This aging routine exceeds industry norms. During the light soaking at 85°C, the device retained 95% (dashed line) of its initial performance.

upon annealing at 100°C, which is needed to fully crystallize the perovskite films. In Fig. 2A, we present the ultraviolet-visible (UV-vis) and photoluminescence (PL) data of the unannealed MAFA and RbCsMAFA films. Whereas MAFA showed several PL peaks with maxima ranging from 670 to 790 nm, the RbCsMAFA film had a narrow peak at 770 nm attributable to perovskite. The insets in Fig. 2A are fluorescence microscopy maps of the surface of the unannealed films, showing that the MAFA films comprise various emissive species that force the preannealed film to crystallize with inhomogeneous starting conditions. However, the RbCsMAFA films were emissive in a narrow range and began to crystallize from more homogeneous conditions. Thus, the addition of the inorganic cations enforced a crystallization that starts with a photoactive perovskite phase (near the final emission after annealing) instead of a mixture of varying emissions that need to converge toward the final emission (see Fig. 2C). These results are consistent with the high reproducibility and lack of yellow phase in the RbCsMAFA films.

Furthermore, we collected the corresponding x-ray diffraction (XRD) data of the unannealed films (Fig. 2B) that showed a pronounced perovskite peak for RbCsMAFA as compared to MAFA films. In Fig. 2, C and D, we show analogous data after annealing, including UV-vis, PL, and XRD data, that reveal a RbCsMAFA band gap of ~1.63 eV (slightly blue-shifted relative to MAFA at ~1.62 eV) containing neither a PbI_2 nor a yellow-phase peak. The low-angle perovskite peaks for MAFA and RbCsMAFA occur at 14.17° and 14.25°, respectively, revealing that Rb indeed modified the crystal lattice. In figs. S5 and S6, we show XRD data of RbMAFA perovskite where we increased the concentration of Rb. We observed, similar to CsMAFA (*9*), that the Pb excess and the yellow-phase impurities of MAFA perovskite disappeared when Rb was added. For Rb_5MAFA, there was a shift to wider angles for the perovskite peak. Moreover, in figs. S7 and S8, we show a series of RbCsMAFA perovskite with an increased amount of Rb together with a $RbPbI_3$ reference. We observed that the perovskite peak shifted to wider angles for Rb_5CsMAFA as well as further suppression of the residual PbI_2 (12.7°) and yellow-phase peak (11.7°) of FA-based perovskite. As more Rb was added, we noted the appearance of a second peak at 13.4° and a double peak at 10.1° that coincide with the peaks for the pure yellow-phase $RbPbI_3$, indicating phase segregation at higher Rb concentrations. This is in good agreement with previous work where a phase segregation was also observed as more and more Cs was added to FA-based perovskite (*8*).

In addition, top-view scanning electron microscopy (SEM) images revealed large crystals in the RbCsMAFA devices (fig. S9), which have been shown to be beneficial for the PV metrics (*19*). Energy-dispersive x-ray spectroscopy measurements (fig. S10) indicated the presence and distribution of Cs and Rb within the perovskite layer.

We collected statistical data on RbCsMAFA devices (with 12 CsMAFA and 17 RbCsMAFA devices measured at a scan rate of 10 mV s^{-1}, without preconditioning such as light soaking or long-term forward voltage biasing; see fig. S11) and observed superior performance relative to CsMAFA. Remarkably, the average V_{oc} increased from 1120 to 1158 mV and the fill factor (FF) increased from 0.75 to 0.78. In Fig. 3A, we show that the best-performing RbCsMAFA cell reached a stabilized power output of 21.6% with FF of 81% and V_{oc} of 1180 mV. The measured short-circuit current density J_{sc} matched the incident photon to current efficiency (IPCE) measurement in fig. S12. We also achieved a stabilized PCE of 19.0% on a large-area 0.5-cm^2 device (see fig. S13).

To correctly determine the value of V_{oc}, we investigated RbCsMAFA devices with the active area being fully illuminated, held at room temperature, and under an inert nitrogen atmosphere. This setup permitted an accurate V_{oc} value without heating or degradation effects (from moisture, for example). In Fig. 3B, for one of our highest-performing devices, we measured an outstanding V_{oc} of 1240 mV, as confirmed by the inset tracking V_{oc} over time. The "loss in potential" (difference between V_{oc} and band gap) is only ~0.39 V, which is one of the lowest recorded for any PV material, implying very small nonradiation recombination losses (*20*). The high V_{oc} is particularly intriguing because this is the major parameter preventing PSCs from reaching their thermodynamic limit (J_{sc} and FF are already approaching their maximal values). Theoretically, in very pure, defect-free materials with only radiative recombination, the loss in potential can be as small as 0.23 V (band gap of 1 eV) to 0.3 V (band gap of 2 eV). In particular, silicon, the main industrial PV material, cannot approach this limit because of its indirect band gap and Auger recombination, exhibiting a loss in potential of ~0.4 V for the most efficient devices (*20*).

The nonradiative recombination losses were quantified by measuring the external electroluminescence quantum efficiency (EQE_{EL}), which is > 1% at a driving current that is equal to the short-circuit current (see Fig. 3C). This value is in the

same order of magnitude and thus consistent with a measured external PL quantum yield of 3.6% for RbCsMAFA (and 2.4% for CsMAFA). Following the approach in (*21*–*25*) [see also fig. S14 and (*18*)], we used the EQE_{EL} and the emission spectrum to predict a V_{oc} value of 1240 mV, confirming independently the value measured from the *J*-*V* curve.

Furthermore, for higher driving currents, the EQE_{EL} in Fig. 3C reaches 3.8%, making the solar cell one of the most efficient perovskite LEDs as well, emitting in the near-infrared/red spectral range (Fig. 3C, inset) (*26*–*28*). Movie S1 shows a RbCsMAFA device mounted in our custom-made device holder. As we tuned toward maximum emission and back, we observed bright EL in daylight. For comparison, for commercially available Si solar cells, $EQE_{EL} \approx 0.5\%$ (*20*). These values for our PSC devices indicate that all major sources of nonradiative recombination were strongly suppressed and that the material has very low bulk and surface defect density. We also investigated transport behavior by means of intensity-modulated photocurrent spectroscopy (IMPS); the findings suggest that the charge transport within the RbCsMAFA perovskite layer is substantially faster than in CsMAFA, which is already much more defect-free than MAFA (*19*) [see also fig. S15 and (*18*)].

Despite the high efficiencies and an outstanding EL, this Rb-containing perovskite material must be able to achieve high stability. This task is not trivial given the hygroscopic nature of perovskite films, phase instabilities, and light sensitivity (*29*). Interestingly, the Achilles' heel of PSCs is not necessarily the perovskite itself, but rather the commonly used spiro-OMeTAD hole transporter material that becomes permeable (at elevated temperature) to metal electrode diffusion into the perovskite, causing irreversible degradation (*30*, *31*). This effect can be mitigated with buffer layers or by avoiding the use of metal electrodes (*30*–*32*). Alternatively, for the combined heat-light stress tests in this work, we found a thin layer of polytriarylamine polymer (PTAA) (see SEM image in fig. S4B) to work equally well (*33*). We imposed the above protocols simultaneously and aged devices for 500 hours at 85°C under continuous illumination with full intensity and maximum power point (MPP) tracking in a nitrogen atmosphere. This compounded stress test exceeds industrial standards (*34*). We show the result in Fig. 3D (red curve). The device started with >17% efficiency at room temperature before the aging protocol was applied (see fig. S16 for non-normalized values of PCE, FF, J_{sc}, V_{oc}, J_{MPP}, and V_{MPP}). During the 85°C step (in which V_{oc} is inevitably lowered), the device retained 95% of its initial performance.

REFERENCES AND NOTES

1. National Renewable Energy Laboratory, Best Research-Cell Efficiencies chart; www.nrel.gov/ncpv/images/efficiency_chart.jpg.
2. N. J. Jeon *et al.*, *Nature* **517**, 476–480 (2015).
3. M. Saliba *et al.*, *Nat. Energy* **1**, 15017 (2016).
4. X. Li *et al.*, *Science* **353**, 58–62 (2016).
5. H. Choi *et al.*, *Nano Energy* **7**, 80–85 (2014).
6. J. W. Lee *et al.*, *Adv. Energy Mater.* **5**, 1501310 (2015).
7. C. Yi *et al.*, *Energy Environ. Sci.* **9**, 656–662 (2016).
8. Z. Li *et al.*, *Chem. Mater.* **28**, 284–292 (2016).
9. M. Saliba *et al.*, *Energy Environ. Sci.* **9**, 1989–1997 (2016).
10. D. P. McMeekin *et al.*, *Science* **351**, 151–155 (2016).
11. H. L. Wells, *Z. Anorg. Chem.* **3**, 195–210 (1893).
12. D. Weber, *Z. Naturforsch. B* **33**, 1443 (1978).
13. D. B. Mitzi, K. Liang, *J. Solid State Chem.* **134**, 376–381 (1997).
14. G. Kieslich, S. J. Sun, A. K. Cheetham, *Chem. Sci.* **5**, 4712–4715 (2014).
15. M. R. Filip, G. E. Eperon, H. J. Snaith, F. Giustino, *Nat. Commun.* **5**, 5757 (2014).
16. F. Hao, C. C. Stoumpos, D. H. Cao, R. P. H. Chang, M. G. Kanatzidis, *Nat. Photonics* **8**, 489–494 (2014).
17. D. M. Trots, S. V. Myagkota, *J. Phys. Chem. Solids* **69**, 2520–2526 (2008).
18. See supplementary materials on *Science* Online.
19. J. P. Correa-Baena *et al.*, *Adv. Mater.* **28**, 5031–5037 (2016).
20. M. A. Green, *Prog. Photovolt. Res. Appl.* **20**, 472–476 (2012).
21. K. Tvingstedt *et al.*, *Sci. Rep.* **4**, 6071 (2014).
22. D. Bi *et al.*, *Sci. Advances* **2**, e1501170 (2016).
23. U. Rau, *Phys. Rev. B* **76**, 085303 (2007).
24. R. T. Ross, *J. Chem. Phys.* **46**, 4590 (1967).
25. W. Tress *et al.*, *Adv. Energy Mater.* **5**, 1400812 (2015).
26. H. Cho *et al.*, *Science* **350**, 1222–1225 (2015).
27. L. Gil-Escrig *et al.*, *Chem. Commun.* **51**, 569–571 (2015).
28. G. Li *et al.*, *Adv. Mater.* **28**, 3528–3534 (2016).
29. N. H. Tiep, Z. L. Ku, H. J. Fan, *Adv. Energy Mater.* **6**, 1501420 (2016).
30. K. Domanski *et al.*, *ACS Nano* **10**, 6306–6314 (2016).
31. K. A. Bush *et al.*, *Adv. Mater.* **28**, 3937–3943 (2016).
32. A. Mei *et al.*, *Science* **345**, 295–298 (2014).
33. J. H. Heo *et al.*, *Nat. Photonics* **7**, 487 (2013).
34. Y. G. Rong, L. F. Liu, A. Y. Mei, X. Li, H. W. Han, *Adv. Energy Mater.* **5**, 1501066 (2015).

ACKNOWLEDGMENTS

M.S. conceived, designed, and led the overall project; M.S., J.-Y.S., A.U., and J.-P.C.-B. conducted SEM, PL, and XRD experiments on the perovskite films; M.S. and W.R.T. performed EL and PL quantum yield experiments; A.U. conducted confocal laser scanning fluorescence microscopy for PL mapping; M.S., K.D., and W.R.T. conducted long-term aging tests on the devices; M.S., T.M., J.-P.C.-B., and A.A. prepared and characterized PV devices; A.H. participated in the supervision of the work; M.G. directed and supervised the research; M.S. wrote the first draft of the paper; and all authors contributed to the discussion and writing of the paper. Supported by the co-funded Marie Skłodowska Curie fellowship, H2020 grant agreement no. 665667 (M.S.); the European Union's Seventh Framework Programme for research, technological development, and demonstration under grant agreement no. 291771 (A.A.); the Swiss National Science Foundation, funding from the framework of Umbrella project (grant agreement nos. 407040-153952, 407040-153990, and 200021-157135/1); the NRP 70 "Energy Turnaround"; the 9th call proposal 906: CONNECT PV; and SNF-NanoTera and the Swiss Federal Office of Energy (SYNERGY). We also acknowledge funding from the European Union's Horizon 2020 program, through a FET-Open Research and Innovation Action under grant agreement no. 687008. A.A. conducted IMPS experiments at the Adolphe Merkle Institute, Fribourg, Switzerland. M.G. and S.M.Z. thank the King Abdulaziz City for Science and Technology for financial support under a joint research project. All data are available in the main paper and supplement. M.S., T.M., K.D., J.-Y.S., S.M.Z., W.R.T., and M.G. are inventors on European Patent Application 1618056.7 submitted by École Polytechnique Fédérale de Lausanne and Panasonic Corporation that covers the perovskite compounds in this work.

SUPPLEMENTARY MATERIALS

www.sciencemag.org/content/354/6309/206/suppl/DC1
Materials and Methods
Supplementary Text
Figs. S1 to S16
Tables S1 and S2
Movie S1
References (*35*–*41*)

18 July 2016; accepted 8 September 2016
Published online 29 September 2016
10.1126/science.aah5557

BIOPHYSICS

Bifurcating electron-transfer pathways in DNA photolyases determine the repair quantum yield

Meng Zhang,[1] Lijuan Wang,[1] Shi Shu,[1] Aziz Sancar,[2] Dongping Zhong[1]*

Photolyase is a blue-light–activated enzyme that repairs ultraviolet-induced DNA damage that occurs in the form of cyclobutane pyrimidine dimers (CPDs) and pyrimidine-pyrimidone (6-4) photoproducts. Previous studies on microbial photolyases have revealed an electron-tunneling pathway that is critical for the repair mechanism. In this study, we used femtosecond spectroscopy to deconvolute seven electron-transfer reactions in 10 elementary steps in all classes of CPD photolyases. We report a unified electron-transfer pathway through a conserved structural configuration that bifurcates to favor direct tunneling in prokaryotes and a two-step hopping mechanism in eukaryotes. Both bifurcation routes are operative, but their relative contributions, dictated by the reduction potentials of the flavin cofactor and the substrate, determine the overall quantum yield of repair.

Photolyases, which belong to the photolyase (PL)–cryptochrome (CRY) superfamily, use a fully reduced flavin ($FADH^-$) cofactor to repair sunlight-induced DNA lesions, including cyclobutane pyrimidine dimers (CPDs) and pyrimidine-pyrimidone (6-4) photoproducts (*1*–*5*). On the basis of sequence analyses, CPD photolyases are highly diversified and can be subdivided into three classes (I to III) (*6*–*8*), as well as single-stranded DNA (ssDNA)–specific PLs (*9*) (Fig. 1A). Thus, the molecular repair

[1]Department of Physics, Department of Chemistry and Biochemistry, and Programs of Biophysics, Chemical Physics, and Biochemistry, The Ohio State University, Columbus, OH 43210, USA. [2]Department of Biochemistry and Biophysics, University of North Carolina School of Medicine, Chapel Hill, NC 27599, USA.
*Corresponding author. Email: zhong.28@osu.edu

Science

Incorporation of rubidium cations into perovskite solar cells improves photovoltaic performance

Michael Saliba, Taisuke Matsui, Konrad Domanski, Ji-Youn Seo, Amita Ummadisingu, Shaik M. Zakeeruddin, Juan-Pablo Correa-Baena, Wolfgang R. Tress, Antonio Abate, Anders Hagfeldt and Michael Grätzel

Science **354** (6309), 206-209.
DOI: 10.1126/science.aah5557originally published online September 29, 2016

Improving the stability of perovskite solar cells

Inorganic-organic perovskite solar cells have poor long-term stability because ultraviolet light and humidity degrade these materials. Bella *et al.* show that coating the cells with a water-proof fluorinated polymer that contains pigments to absorb ultraviolet light and re-emit it in the visible range can boost cell efficiency and limit photodegradation. The performance and stability of inorganic-organic perovskite solar cells are also limited by the size of the cations required for forming a correct lattice. Saliba *et al.* show that the rubidium cation, which is too small to form a perovskite by itself, can form a lattice with cesium and organic cations. Solar cells based on these materials have efficiencies exceeding 20% for over 500 hours if given environmental protection by a polymer coating.

Science, this issue pp. 203 and 206

Science (print ISSN 0036-8075; online ISSN 1095-9203) is published by the American Association for the Advancement of Science, 1200 New York Avenue NW, Washington, DC 20005.